AGU PUBLICATIONS

JGR

Journal of Geophysical Research: Space Physics

RESEARCH ARTICLE
10.1002/2016JA023397

# A statistical study of magnetospheric electron density using the Cluster spacecraft

**J. K. Sandhu[1], T. K. Yeoman[1], R. C. Fear[1,2], and I. Dandouras[3,4]**

[1]Department of Physics and Astronomy, University of Leicester, Leicester, UK, [2]Now at Department of Physics and Astronomy, University of Southampton, Southampton, UK, [3]University of Toulouse, UPS-OMP, IRAP (Institut de Recherche en Astrophysique et Planétologie), Toulouse, France, [4]CNRS, IRAP, Toulouse, France

**Key Points:**
- WHISPER/Cluster observations used to determine empirical electron density model
- Observed enhancement in total electron density field line distribution, localized to equator
- Empirical models describing number density and ion composition used to determine empirical mass density model

**Supporting Information:**
- Supporting Information S1
- Figure S1
- Figure S2
- Figure S3
- Figure S4

**Correspondence to:**
J. K. Sandhu,
js423@le.ac.uk

**Citation:**
Sandhu, J. K., T. K. Yeoman, R. C. Fear, and I. Dandouras (2016), A statistical study of magnetospheric electron density using the Cluster spacecraft, *J. Geophys. Res. Space Physics*, *121*, 11,042–11,062, doi:10.1002/2016JA023397.

Received 26 AUG 2016
Accepted 6 NOV 2016
Accepted article online 15 NOV 2016
Published online 22 NOV 2016



**Abstract** Observations from the WHISPER (Waves of High frequency and Sounder for Probing of Electron density by Relaxation) instrument on board Cluster, for the interval spanning 2001–2012, are utilized to determine an empirical model describing the total electron density along closed geomagnetic field lines. The model, representing field lines in the region of $4.5 \leq L < 9.5$, includes dependences on $L$ and magnetic local time. Data verification tests ensured that the WHISPER data set provided unbiased measurements for low-density regions, including comparisons with Plasma Electron and Current Experiment and Electric Field and Waves observations. The model was determined by modeling variations in the electron density along the field lines, which is observed to follow a power law distribution along the geomagnetic field at high latitudes, with power law index values ranging from approximately 0.0 to 1.2. However, a localized peak in electron density close to the magnetic equator is observed, which is described using a Gaussian peak function, with the electron density peak ranging as high as 10 $cm^{-3}$ above the background power law dependence. The resulting model illustrates some key features of the electron density spatial distribution. The role of the number density distribution, represented by the empirical electron density model, in determining the total plasma mass density is also explored. By combining the empirical electron density model with an empirical average ion mass model, the total plasma mass density distribution is inferred, which includes contributions of both the number density and ion composition of the plasma in the region.

## 1. Introduction

Plasma mass density is a fundamental parameter of the magnetosphere, and variations in the plasma mass density provide information on magnetospheric morphology and dynamics. Furthermore, the mass density plays a role in the determination of wave mode propagation, important for radiation belt energization and decay [*Meredith et al.*, 2003; *O'Brien et al.*, 2003], as well as reconnection rates [*Borovsky and Denton*, 2006]. A key motivation for developing magnetospheric mass density models is to estimate the frequencies of ultralow frequency waves, corresponding to the response time of the magnetosphere to perturbations. The mass density of the plasma is dependent on the number density of the electrons and ions, in addition to the ion composition. A previous study developed an empirical model for the average ion mass, for closed field lines in the range of $5.9 \leq L < 9.5$, over all magnetic local time (MLT), describing the ion composition contribution to the total plasma mass density. This study aims to determine a corresponding empirical model of the spatial distribution of total plasma electron density for the closed magnetosphere, in a region covering the outer plasmasphere, plasmatrough, and near-Earth plasma sheet. The resulting model will describe variations in the electron density in the equatorial plane and along magnetic field lines.

Variations in electron density along closed magnetospheric field lines have often been assumed to follow a power law dependence. *Cummings et al.* [1969] is an example of this case, where assuming a dipolar field and hydrogen plasma, the electron density distribution along the geomagnetic field was modeled as a power law function. This model states that the electron density, $n_e$, at a radial distance $R$ ($R_E$), on a field line with a maximum radial distance of $L$ ($R_E$) is given by

$$n_e = n_{e0}\left(\frac{L}{R}\right)^{\alpha} \tag{1}$$

where $n_{e0}$ is the electron density at $R = L$, and $\alpha$ is termed the power law index. This form implies that the electron density is a minimum at the magnetic equatorial position along the field line and increases with

magnetic latitude toward the ionospheric ends of the field line, assuming that $\alpha$ is positive. The rate at which the electron density increases depends on the magnitude of the power law index, $\alpha$.

Previous work has produced empirical models describing the spatial variations in the total plasma electron density for the closed magnetosphere [*Carpenter and Anderson*, 1992; *Fung et al.*, 2001; *Goldstein et al.*, 2001; *Sheeley et al.*, 2001; *Denton et al.*, 2002, 2004], which are now briefly reviewed. These studies determine the total electron density of the local plasma through measurements of plasma characteristic frequencies using in situ spacecraft observations. Many empirical models, based on the electron density observations, are focused on quantifying the distribution of electron density in the equatorial plane [*Carpenter and Anderson*, 1992; *Fung et al.*, 2001; *Sheeley et al.*, 2001; *Denton et al.*, 2004; *Berube et al.*, 2005]. *Fung et al.* [2001] and *Berube et al.* [2005] presented a model for plasma electron density, representing the region of $2 < L < 5$, based on observations from the Radio Plasma Imaging instrument, on board the IMAGE spacecraft, between May 2000 and May 2001. Similarly, *Denton et al.* [2004] utilized upper hybrid resonance frequency measurements from PWI (Plasma Wave Instrument) on board Polar obtained between March 1996 to September 1997, to determine an empirical electron density model. The model covers $2.5 < L < 8.0$. As well as limited temporal coverage of the data sets, these models [*Fung et al.*, 2001; *Denton et al.*, 2004; *Berube et al.*, 2005] do not quantify any variations in electron density with MLT (magnetic local time). A study by *Carpenter and Anderson* [1992] developed a model based on electron density values using measurements from the SFR (Sweep Frequency Receiver) instrument on board ISEE (International Sun-Earth Explorer) 1, observed during 1977–1983. The model accounted for some variations with MLT, comparing spatial distributions for $0000 \leq \text{MLT} \leq 0600$ and $0600 \leq \text{MLT} \leq 1500$, considering $L$ values in the range of 2.25 to 8. However, full MLT coverage is not provided, and the equatorial variations of electron density in the region of $1500 \leq \text{MLT} \leq 0000$ are not quantified. In contrast, *Sheeley et al.* [2001] determined an empirical model for equatorial variations in electron density, for $3 \leq L \leq 7$, including variations in electron density with MLT. The model was based on observations by the SFR (Sweep Frequency Receiver) instrument on board CRRES (combined Release and Radiation Effects Satellite) during July 1990 to October 1991.

As well as describing variations in the equatorial plane, dependences along field lines of electron density have been quantified by previous studies. Variations along closed geomagnetic field lines were examined in a study conducted by *Goldstein et al.* [2001], where the gradient of electron density was empirically modeled for $2.5 \leq L \leq 6.3$. The model was based on observations of the upper hybrid frequency measured by PWI on board the Polar spacecraft, obtained during March 1996 to September 1997. However, this study imposed an assumption that the variations of electron density along the field line follow the simplistic power law dependence (equation (1)). Furthermore, dependences on MLT were not included, the data set had relatively limited temporal coverage, and equatorial variations in electron density were neglected. A subsequent study by *Denton et al.* [2002], using the same data set as *Goldstein et al.* [2001], included both equatorial and variations along the field lines, describing the spatial distribution of the total electron density for $3.5 \leq L \leq 7.8$. Although this study provides a useful description of the plasma number density, the key constraint of the empirical model is that MLT dependences are neglected. Furthermore, the data set covers a short time interval, relative to the solar cycle, thus restricting the model in terms of variations with solar phase.

From a survey of existing electron density models, it is apparent that no sufficiently detailed description of the variations in the closed magnetosphere exist, with good spatial and temporal coverage. This study improves on previous models by using a larger data set, providing statistically significant results with good spatial coverage. In addition, both variations along magnetic field lines, including dependences with both $L$ and MLT will be included.

## 2. Instrumentation

This study utilizes data observed by the four identical Cluster spacecraft (C1, C2, C3, and C4). The four spacecraft, arranged in a tetrahedral configuration, have a polar orbit, allowing them to sample many key regions of the magnetosphere [*Escoubet et al.*, 1997a]. Therefore, Cluster is suitable for providing the necessary data coverage required for this study. The electron density data set, obtained from the Cluster Science Archive, covers the time interval of 2001–2012.

Electron density data are provided by the WHISPER (Waves of High frequency and Sounder for Probing of Electron density by Relaxation) instrument on board all four of the spacecraft. This instrument was chosen

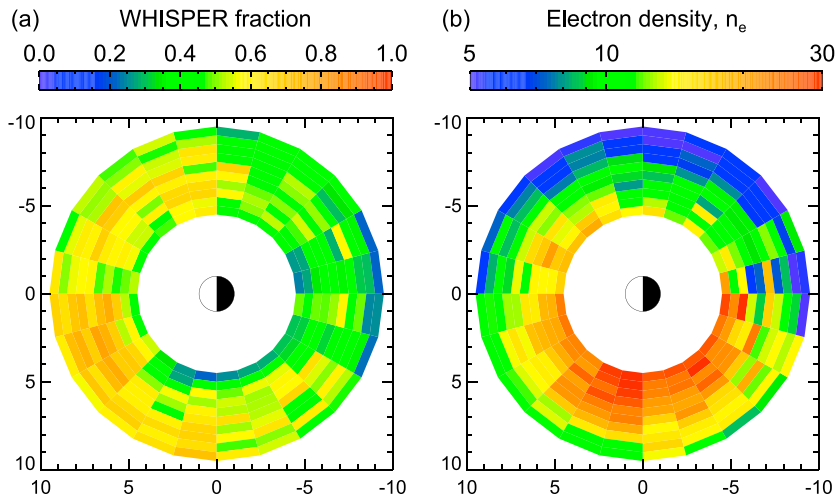


**Figure 1.** Polar plots showing distributions in L-MLT space, where values are binned for field line *L* value (using a bin width of 0.5) and MLT (using a bin width of 1 h). The plots show the average of values within each bin. (a) The fraction of the total spacecraft passes where WHISPER data is available. (b) The distribution of total electron density, $n_e$ ($cm^{-3}$), as measured by WHISPER.

over the electron analyzer PEACE (Plasma Electron and Current Experiment) on board Cluster, as PEACE density estimates are sensitive to photoelectron contamination [*Johnstone et al.*, 1997]. WHISPER is a resonance sounder that measures the total electron density of the local plasma using its active mode [*Décréau et al.*, 1997]. This involves identifying the frequency of the electron plasma frequency, $f_{pe}$, allowing the electron plasma density, $n_e$, to be directly inferred [*Trotignon et al.*, 2001, 2003], using the relation

$$n_e = \frac{\epsilon_0 m_e}{e^2}\left(2\pi f_{pe}\right)^2 \simeq \frac{1}{81} f_{pe}^2 \tag{2}$$

The frequency range covered by WHISPER restricts the electron density range of the measurements to within 0.25–80 $cm^{-3}$ [*Trotignon et al.*, 2001].

*Laakso et al.* [2002] note that the resonance sounding technique employed by WHISPER to measure the total electron density may not be suitable for tenuous plasmas where the density is extremely low. For these regions, such as in the polar cap, the plasma waves may not be identifiable from the spectra, and the total electron density cannot be determined. Therefore, it is important to assess whether the WHISPER observations for the region considered in this study are systematically biased such that higher density measurements are preferentially obtained. Figure 1a shows the fraction of observations obtained by the WHISPER instrument binned for *L* value (refer to section 3 for the details on determining the *L* value corresponding to a measurement) and MLT, with values within each bin averaged. The fraction of measurements is defined as the fraction of spacecraft passes through an L-MLT bin where WHISPER observations of the total electron density are obtained. In order to assess whether there is a significant systematic bias related to the capability of the WHISPER instrument to return measurements of the total electron density for nightside MLT sectors, the fraction of WHISPER observations shown in Figure 1a can be compared to the electron density distribution, as shown in Figure 1b. Figure 1b shows, using the same approach as Figure 1a, electron density observations binned for *L* value and MLT, where values in each bin are averaged. Figure 1b clearly shows that the total electron density observed by WHISPER shows reduced values on the dawnside compared to the duskside (note that the details concerned with this feature will be discussed in section 5). A comparison between Figure 1a and Figure 1b does not show any evidence of WHISPER preferentially returning observations for high-density regions compared to low-density regions. This can be assessed further by considering the correlation of the bins shown in Figures 1a and 1b, and the results show that the Pearson's correlation coefficient for WHISPER fraction as a function of electron density is −0.07. This indicates that there is an extremely weak correlation between the two quantities (in fact, the sign of the correlation coefficient suggests increased WHISPER fractions in low-density regions, opposite to the expected dependence). Therefore, there is no evidence for any systematic bias in the WHISPER observations for the region considered in this study.

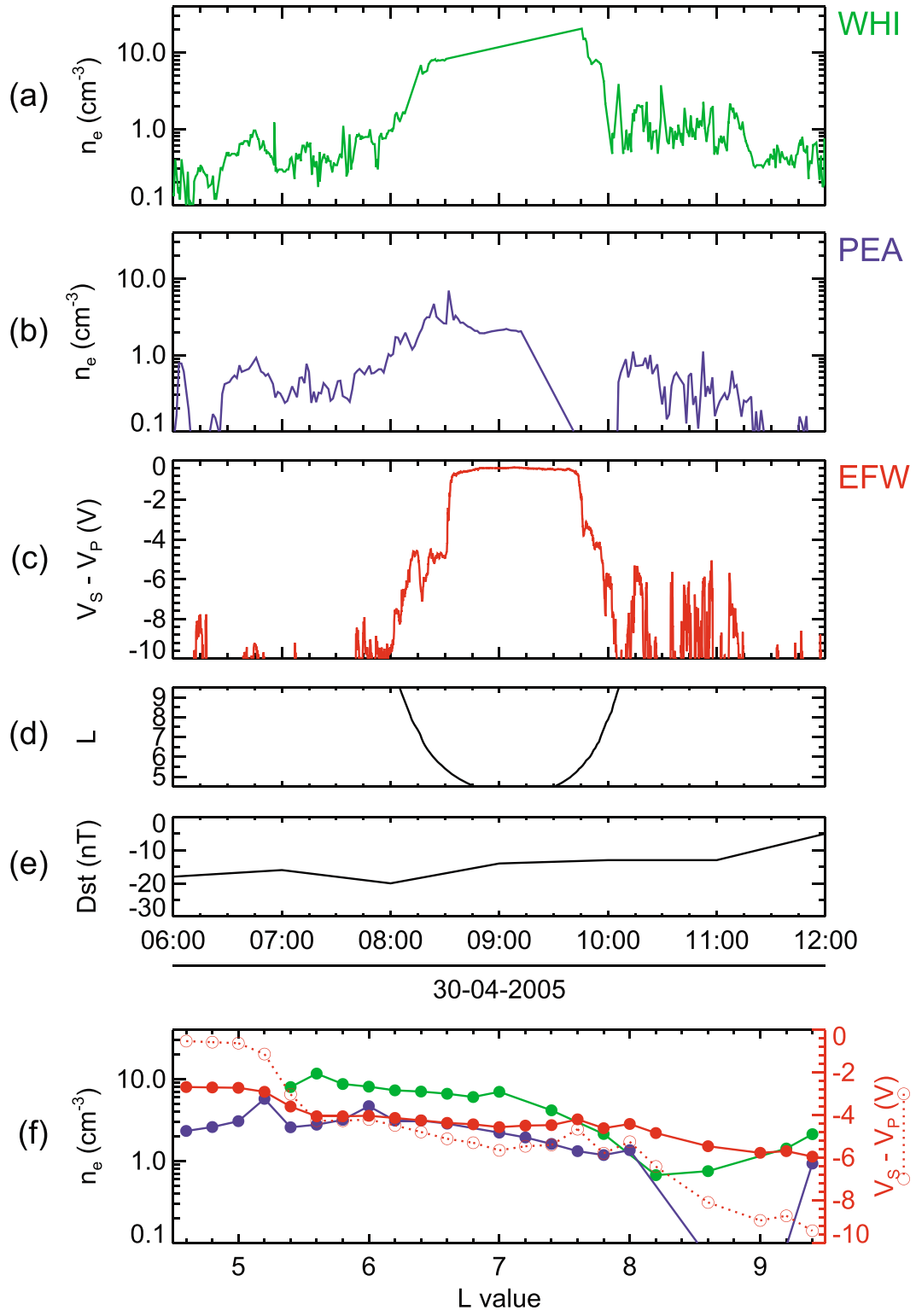


**Figure 2.** WHISPER (green), PEACE (blue), and EFW (red) observations obtained by C1 during the perigee pass of orbit 745. Electron density, $n_e$ ($cm^{-3}$) time series for the (a) WHISPER and (b) PEACE instruments. (c) The spacecraft potential, $V_S - V_P$ ($V$) time series. The spacecraft (d) $L$ value and (e) $Dst$ index (nT) variation. (f) For the observations of each instrument, the data are binned for $L$ value, using a bin size of 0.2, and averaged. The solid profiles correspond to electron density, and the dotted profile corresponds to spacecraft potential. Electron density measurements for the EFW instrument were inferred from spacecraft potential measurements using relations from *Lybekk et al.* [2012].

Furthermore, to assess whether the spatial variations in electron density observed by WHISPER are representative of the plasma, comparisons with PEACE (Plasma Electron and Current Experiment) and EFW (Electric Field and Waves) data have been performed for multiple case studies. The electron spectrometer, PEACE, provides direct measurements of the electron density for particles with energies in the range of 0.59–9.45 eV [*Johnstone et al.*, 1997]. Conversely, the EFW instrument observes the spacecraft potential relative to the plasma [*Gustafsson et al.*, 1997, 2001], which can be related to the local electron density using relations determined by *Lybekk et al.* [2012]. The spacecraft potential technique for monitoring electron density is ideal for tenuous plasma environments and has been previously employed to observe regions such as the cusp and magnetotail lobes [*Pedersen*, 1995; *Escoubet et al.*, 1997b; *Laakso and Pedersen*, 1998; *Nakagawa et al.*, 2000; *Scudder et al.*, 2000; *Pedersen et al.*, 2001; *Laakso et al.*, 2002; *Pedersen et al.*, 2008; *Lybekk et al.*, 2012]. Figure 2 shows data obtained by C1 for the perigee pass of orbit 745, from the WHISPER, PEACE, and EFW instruments, for a representative case study. Figures 2a and 2b show electron density observations from WHISPER and PEACE, respectively, and Figure 2c shows spacecraft potential observations from EFW. The *L* value corresponding to the spacecraft position is indicated in Figure 2d, and the level of geomagnetic activity for the interval is described by the *Dst* index time series in Figure 2e. The WHISPER, PEACE, and EFW data sets were binned for *L* value, using a bin size of 0.2, averaged, and plotted as a function of *L* in Figure 2f, for the *L* range of interest. The solid colored profiles show the electron density variation as measured by WHISPER (green), PEACE (blue), and inferred values from EFW (red) using the *Lybekk et al.* [2012] relations. The dotted red profile shows the spacecraft potential observed by EFW, from which electron density values were inferred. It is noted that the magnitude of the spacecraft potentials observed here, representative for this region, are relatively small compared to the range of values typically used for the spacecraft potential technique and lie outside the range appropriate for inferring electron densities. This suggests that the WHISPER instrument is more suitable, compared to the EFW instrument, for monitoring electron density for this region. Regardless, a comparison of the electron density profiles indicates generally good agreement between each instrument data set, with similar *L* gradients. As expected, the magnitude of electron density observed by PEACE, corresponding to a restricted energy range, is lower than the total electron density measured by WHISPER. Overall, the representative example shown in Figure 2 provides evidence that the WHISPER data set should provide a valid electron density spatial distribution for the region considered in this study.

## 3. Data Reduction

In order to examine the spatial variations in the electron density, the same technique is used as for the previous study [*Sandhu et al.*, 2016], which will now be briefly summarized here for completeness. Considering each orbit individually, the data are binned by position in $0.5 \times 0.5 \times 0.5$ $R_E$ bins, where the GSM (Geocentric Solar Magnetospheric) coordinate system is employed. The observations in each bin, typically ranging between 10 and $10^2$, are used to determine the average value and average time of measurement. In addition, the position of the bin is used to identify the corresponding MLT. Over all orbits used in this study, the total number of passes through each position bin is typically of the order $10^2$.

For each position bin, the corresponding *L* value is determined. The *L* value is defined as the radial distance that the bin's field line crosses the magnetic equatorial plane. As described by *Sandhu et al.* [2016], the T96 magnetic field model [*Tsyganenko*, 1996] is used to trace the field line corresponding to the bin's position and the average measurement time. The T96 magnetic field model is parameterized by the solar wind dynamic pressure, IMF (Interplanetary Magnetic Field) $B_y$ and $B_z$ components, and the *Dst* index, and the parameter values corresponding to the average measurement time of each bin were used in the field line tracing. Hourly averaged *Dst* values were obtained from the World Data Center for Geomagnetism (Kyoto) data set, and 1 min averaged solar wind parameters were obtained from the NASA/Goddard Space Flight Center OMNI data set through OMNIWeb.

As this study aims to consider only the closed region of the magnetosphere, any points where the corresponding field line is traced as open by the T96 magnetic field model is removed from the data set. However, due to occasional inaccuracies in the T96 magnetic field model, some measurements located on an open field line may by traced as closed. It was identified that this effect contributed to some discrepancies in the data set, particularly for points located close to the dayside magnetopause. In order to verify whether a bin's field line is closed, a method adapted from *Clausen et al.* [2009] is used, which is now briefly described. Full details on the method are described by *Sandhu et al.* [2016]. Using DEF (Differential Energy Flux)

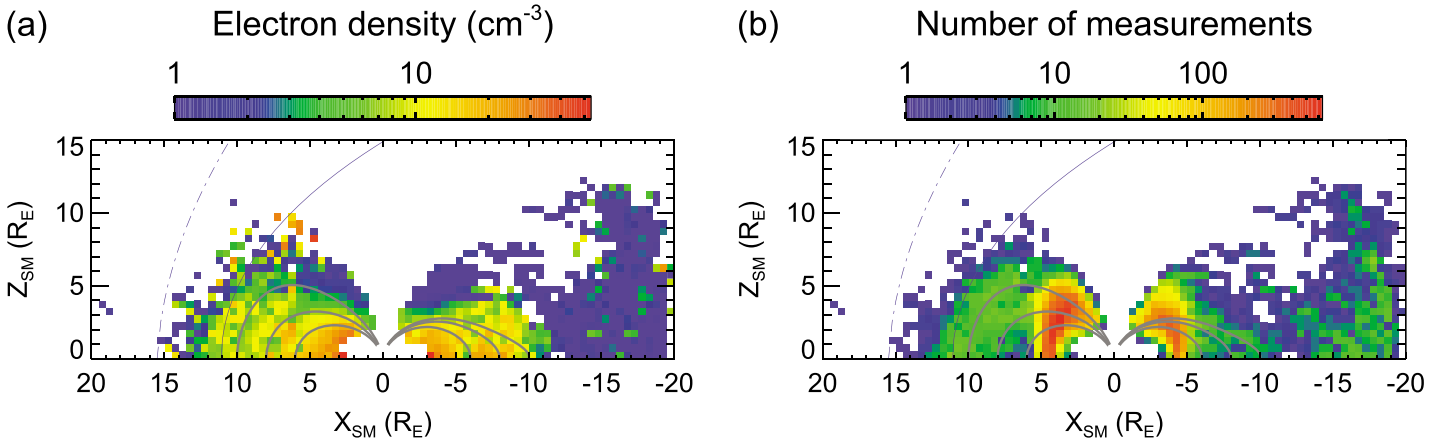


**Figure 3.** Spatial distribution of (a) average electron density ($cm^{-3}$) and (b) the number of measurements obtained by WHISPER in the *X-Z* plane (SM coordinate system). The grey lines show reference T96 model magnetic field lines in the noon and midnight meridian planes, corresponding to spring equinox with a solar wind dynamic pressure of 2 nPa, for *L* values of 6, 8, and 10.

measurements obtained by the Hot Ion Analyzer instrument [*Rème et al.*, 1997] on board Cluster, empirically defined thresholds are used to identify plasma with DEF values characteristic of magnetosheath plasma. Points are defined as being on closed field lines if they have a DEF of ions at 0.7 keV below the critical value of $1 \times 10^7$ keV $cm^{-2}$ $s^{-1}$ $sr^{-1}$ $keV^{-1}$ or a DEF of ions at 0.02 keV above $6 \times 10^6$ keV $cm^{-2}$ $s^{-1}$ $sr^{-1}$ $keV^{-1}$. By applying the method to all points in the data set, any points identified to be on open field lines are discarded, and a reduction in discrepancies located close to the OCB (Open-Closed Boundary) is observed.

The resulting electron density data set, where values have been binned for position and the corresponding MLT and *L* values evaluated, is now presented. Using the same approach as *Sandhu et al.* [2016], a coordinate transformation is applied to determine the bins' position in the SM (Solar Magnetic) coordinate system, considering each orbit individually. The distribution of average electron density values in the *X-Z* SM plane is shown in Figure 3a, illustrating variations in the WHISPER data set with magnetic latitude and *L* value. The color of the points represent the average values over all orbits, binned spatially with a bin size of 0.5 $R_E$. Measurement positions have been azimuthally mapped about the *Z* axis into the noon-midnight meridian, averaging over dayside and nightside MLT sectors separately. Furthermore, measurements in the Southern Hemisphere are mapped to the corresponding position in the Northern Hemisphere, assuming that the distribution along the geomagnetic field is hemispherically symmetric.

Figure 3b shows the corresponding spatial distribution of the number of measurements in each position bin, mapped to the *X-Z* SM plane. It can be seen that the WHISPER data set contains a sufficient number of measurements over a range of *L* values in order to provide a statistically significant and reliable description of the electron density spatial distribution.

## 4. Electron Density Distribution Along the Magnetic Field

The electron density data set, from measurements obtained by WHISPER, provides sufficient spatial coverage along field lines in the region spanning $4.5 \leq L < 9.5$. This corresponds predominantly to the outer plasmasphere, plasmatrough, and near-Earth plasma sheet. The following analysis considers the distribution of electron density along magnetic field lines in this region, including a comparison of data at different *L* and MLT values.

In order to determine the distribution of electron density along field lines, the same approach as used by *Sandhu et al.* [2016] is applied to the electron density data set, with a summarized description provided here. The method involves identifying an appropriate functional form to represent the distribution of electron density along the geomagnetic field. A hierarchical least squares fitting technique [*Clark and Gelfand*, 2006; *Tabachnick and Fidell*, 2006] is used to obtain a model function, where the function parameters include dependences on *L* and MLT.

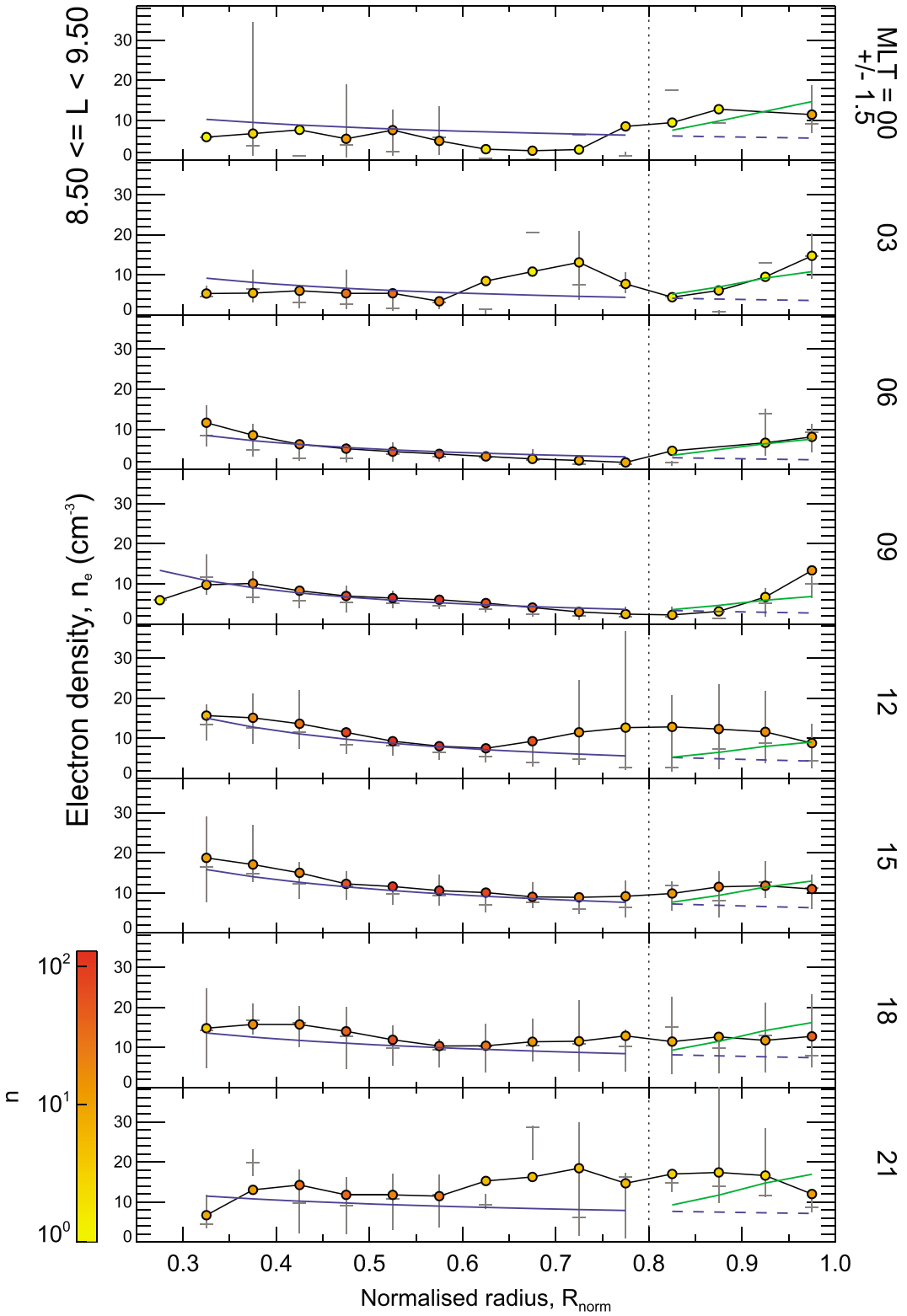


**Figure 4.** Electron density, $n_e$ ($cm^{-3}$) plotted as a function of normalized radius, $R_{norm}$, for $8.5 \leq L < 9.5$ at 3 h MLT intervals, where the color of each point indicates the number of WHISPER measurements, $n$, averaged in each bin. The upper and lower quartiles of the distribution of points averaged in each bin is shown by the grey line, intersected by a short horizontal line at the median value. The vertical dashed line indicates the boundary between the power law and Gaussian dependences. The blue line represents the best fitting power law dependence, where the dashed blue line is the extrapolated dependence. The green line represents the best fitting Gaussian function.

Similarly to *Sandhu et al.* [2016], the electron density data are binned for the field line $L$ value using a bin size of 1, binned for MLT using a bin size of 3 h, and binned for the normalized radius, $R_{norm}$ using a bin size of 0.05. The normalized radius is defined as the radial distance at which a measurement was obtained, $R\,(R_E)$, divided by the $L$ value of the field line. An example plot showing the electron density as a function of normalized radius is shown in Figure 4 for binned data corresponding to an $L$ shell of 9. Each point represents the average electron density value in the bin, and the color of the point corresponds to the number of averaged measurements in each bin, $n$. The vertical panels show the density data for each MLT bin. The interquartile range of electron density values in each bin is indicated by the vertical grey lines, which extend from the lower quartile to the upper quartile. The median value of each bin is indicated by the short horizontal grey line. It is noted here that the profiles are smoothed using a boxcar function with a width of three bins, and consequently, some points are shifted relative to the grey lines. Figure 4 shows that at higher magnetic latitudes (equivalently, lower $R_{norm}$ values), the distribution tends to resemble that of the expected power law (see equation (1), previously discussed in section 1), as evidenced by the blue curve, which represents a power law best fit described in more detail in the following subsection. However, at lower magnetic latitudes (higher $R_{norm}$ values), close to the magnetic equatorial plane, a peak in electron density is often observed, which appears to have an MLT dependence. To account for the different dependences observed, the distribution along field lines is separated into two regions, where the boundary between these regions is indicated by the vertical dotted line in Figure 4. The value of the normalized radius at the boundary between the two dependences is defined as $R_{norm} = 0.8$, which is determined from the mean value of $R_{norm}$ where the average electron density is at a minimum for the field line distribution.

### 4.1. Power Law Model

For the high magnetic latitude region, a power law dependence is apparent, so the functional form of equation (1) is chosen to describe the distribution along the magnetic field. Using a least squares fitting method, weighted by the number of measurements in each bin, the best fit parameters ($n_{e0}$ and $\alpha$) in equation (1) are determined for each distribution. The least squares fitting has been weighted by the number of measurements in each bin, as the electron density is known to be variable in this region. Therefore, the weighting is estimated from the number of measurements in order to avoid the fit being distorted by values that are not representative of the typical distribution. Variations in the best fit parameters are then quantified to include dependences with $L$ and MLT, providing a hierarchical model for a power law distribution along field lines. The resulting power law model is shown below in equation (3), with model parameters given by equations (3c) and (3d):

$$n_e = n_{e0} {R_{norm}}^{-\alpha} \qquad R_{norm} \le 0.8 \tag{3a}$$

$$= a \exp\left[-\frac{1}{2}\left(\frac{R_{norm} - 1.0}{0.1}\right)^2\right] + n_{e0} \qquad R_{norm} > 0.8 \tag{3b}$$

$$n_{e0} = 35.0 - 3.35L + (9.38 - 0.756L)\cos(15\text{MLT} + 76.0) \tag{3c}$$

$$\alpha = -0.173 + 0.113L + 0.412\cos(15\text{MLT} + 81.9 + 16.0L) \tag{3d}$$

$$a = -1.24 + 0.944L + 2.92\cos(15\text{MLT} + 40.0) \tag{3e}$$

This power law model is shown as the solid blue line in Figure 4, and the model has also been extrapolated into the lower latitude region for comparison, as illustrated by the dashed blue line. Due to the hierarchical technique used here, the model fits shown in Figure 4 are results of a fit to the data set as a whole, accounting for variations with $L$ and MLT, as opposed to an individual $L$-MLT bin. As such, some MLT sectors may not appear to represent a least squares fit for the individual profiles (e.g., Figure 4, first panel). This approach was employed here as the modeling technique provides a description of the global, large-scale spatial variations in the data set, accounting for dependences with $L$ and MLT.

The functional form used for all model parameters combines a sinusoidal function, to represent the MLT dependence, with an offset to represent the mean value across MLT variations. Further details on the form of the functions are described by *Sandhu et al.* [2016]. The sinusoidal component includes a phase term, describing the MLT location of peak parameter values, and an amplitude term to describe the magnitude

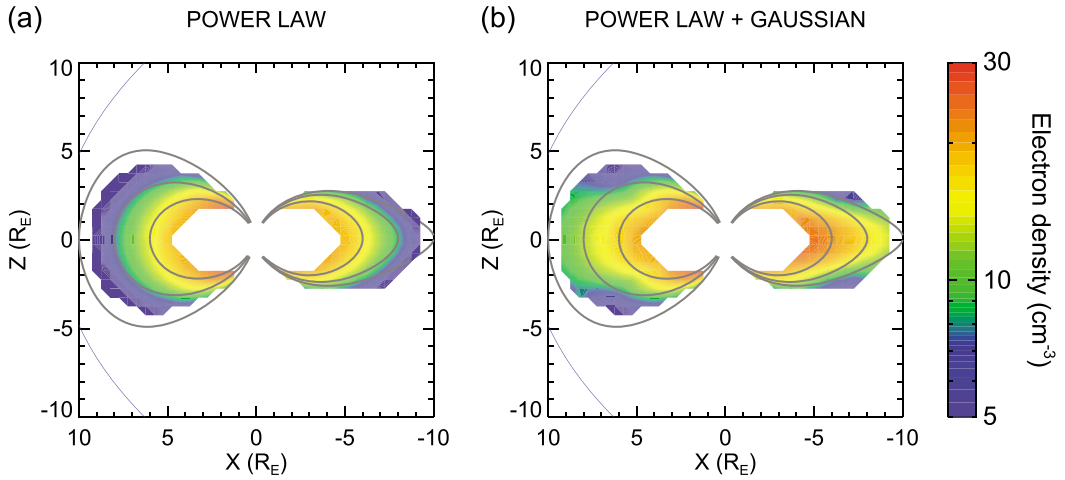


**Figure 5.** Spatial distribution in the *X*-*Z* SM plane using the model for electron density ($cm^{-3}$). The distributions using both (a) the extrapolated power law form and (b) Gaussian function for the low-latitude electron density dependence are shown for comparison. Note that the scales have been adjusted relative to the data plots (Figure 3) to focus on the most relevant regions. The grey lines show reference magnetic field lines in the noon and midnight meridian planes, for *L* values of 6, 8, and 10. The T96 magnetic field model used in this case corresponds to spring equinox, with a solar wind dynamic pressure of 2 nPa.

of MLT asymmetries. The phase, amplitude, and offset terms are defined as linear functions of *L*, unless a clear dependence on *L* was not identifiable from the parameter variations.

The key features of the power law dependence, and the variations with *L* and MLT, are discussed in section 5.

### 4.2. Gaussian Model

The localized peak in electron density in the lower latitude region indicates that a power law dependence is not an appropriate form to describe the variations in this region, as can be seen from the difference between the extrapolated power law model and observed electron density in Figure 4 close to the magnetic equator (at $R_{norm} > 0.8$). For this region, a Gaussian function is chosen to represent the electron density peak. The width of the peak is fixed to 0.1 and the position to $R_{norm} = 1.0$ (i.e., at the magnetic equatorial plane), in order to reduce the number of free parameters in the fitting. An offset, equal to $n_{e0}$ from the power law model defined in equation (3c), is added to the Gaussian function. This is done so that the electron density given by the Gaussian function is representing an enhancement compared to the background power law model, extrapolated into the lower latitude region. This region is modeled by fitting a Gaussian function to the distributions along the field line, using a least squares method weighted by the number of measurements in each bin, and quantifying the parameters' dependence on *L* and MLT. The resulting model for this region is shown in equation (3b), where $n_{e0}$ and $a$ (peak height above $n_{e0}$) are defined in equations (3c) and (3e). Further discussion of the dependences present in this model are included in section 5.

The power law and Gaussian models can now be combined to form the model for the electron density distribution along field lines, with dependences on *L* and MLT included, as summarized in equation (3). The azimuthally mapped spatial distribution (averaging separately over dayside and nightside MLT sectors) predicted by the resulting model is shown in Figure 5 in the *X*-*Z* SM plane, including the distribution where the equatorial peak is neglected by using the extrapolated power law form for the lower latitude region (Figure 5a). A comparison of the two forms of the model show that the inclusion of the Gaussian function to represent the localized peak results in significant enhancements in electron density at low latitudes, as expected, particularly for large L values with the effect being stronger on the nightside.

The spatial distribution in the T96 magnetic equatorial plane predicted by the electron density model is shown in Figure 6, illustrating MLT and *L* dependences. Figure 6a corresponds to the extrapolated power law model and Figure 6b corresponds to the combination of the power law and Gaussian functions. A comparison of the distributions further illustrate how the use of the Gaussian function, accounting for the localized peak in electron density, results in increased values overall compared to the extrapolated power law form.

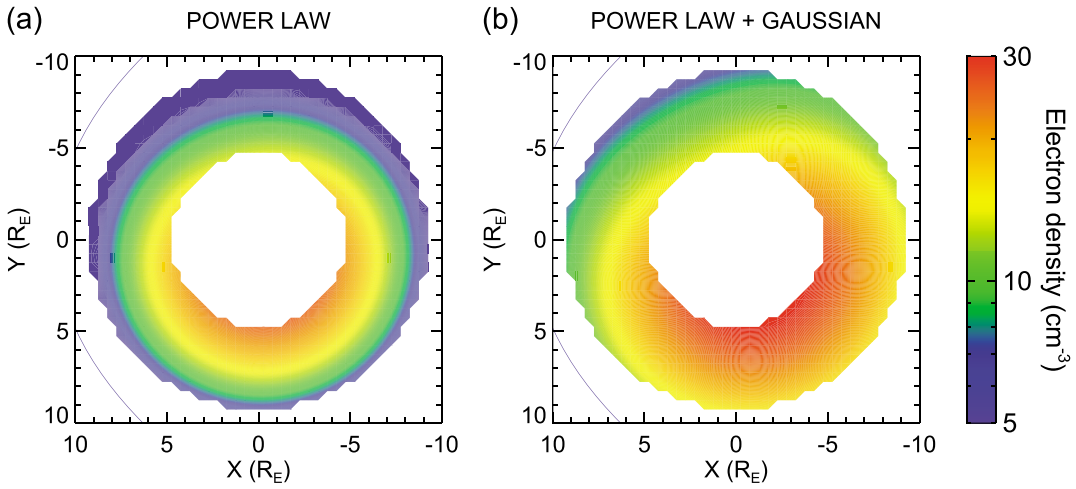


**Figure 6.** The spatial distribution of electron density ($cm^{-3}$) in the T96 magnetic equatorial plane, in the same format as Figure 5.

## 5. Discussion

An empirical model describing variations in electron density along the magnetic field, including dependences on both *L* and MLT, has been obtained (section 4). The key features of the model are now discussed in further detail, providing information on the processes influencing the electron density spatial distribution in the considered region of the closed magnetosphere.

### 5.1. Electron Density

A comparison of the equatorial electron density values observed here to results from previous studies indicate some important differences, which are now briefly summarized. Many previous results appear to observe lower electron densities [*Denton et al.*, 2004; *Lointier et al.*, 2013; *Takahashi et al.*, 2014; *Sheeley et al.*, 2001]; however, there are several significant factors that may account for the apparent discrepancies. The study conducted by *Sheeley et al.* [2001] quantified electron density variations for the plasmasphere and plasmatrough regions. Whereas the empirical model developed here determined an electron density value of 25.3 $cm^{-3}$ at $L = 5$ for the midnight meridian, the results of *Sheeley et al.* [2001] suggest that values should be around 120 $cm^{-3}$ for the plasmasphere region and approximately 12 $cm^{-3}$ for the plasmatrough region. A closer agreement is observed for other MLT sectors. The difference in equatorial electron density values can be attributed to the method employed in this study, where plasmasphere and plasmatrough are not separated. Results may also be compared to the findings of *Denton et al.* [2004], where plasmatrough measurements indicate significantly lower equatorial electron densities compared to the values obtained in this study. Specifically, at an *L* value of 6, *Denton et al.* [2004] observed an equatorial electron density of ~10 $cm^{-3}$, compared to ~19 $cm^{-3}$ for the empirical model presented here, averaging over all MLT to allow an equivalent comparison. A key feature of the *Denton et al.* [2004] methodology is the assumed power law distribution along field lines, which was combined with off-equatorial measurements of the electron density using the PWI instrument on board the Polar spacecraft. Therefore, the low-latitude equatorial region was not sampled, neglecting the equatorial enhancement in electron density and underestimating the equatorial electron density. Comparing results with our empirical model using an extrapolated power law, thus neglecting the equatorial enhancement, provides an equatorial electron density of ~15 $cm^{-3}$ and is in closer agreement with the *Denton et al.* [2004] value. Furthermore, the results of *Denton et al.* [2004] represent solar minimum conditions, corresponding to lower electron density values due to relatively decreased ionization, whereas these results presented here represent a wider range of solar activity levels. Following studies, in particular, *Lointier et al.* [2013] and *Takahashi et al.* [2014], also observed lower equatorial electron densities compared to the results of this empirical electron density model. However, similarly to *Denton et al.* [2004], *Takahashi et al.* [2014] assumed a power law distribution along field lines, neglecting any equatorial enhancement. The data set employed by *Lointier et al.* [2013] exhibits a lack of data coverage near the equator, and *Lointier et al.* [2013] emphasize that the values mapped to the equatorial plane have not accounted for variations in electron density along the field, and therefore do not represent true equatorial values. Consequently, it can be expected that values will be

underestimated, due to the presence of an enhancement localized at the magnetic equator. Overall, differences between the empirical model values of equatorial electron density and the results of previous studies [*Denton et al.*, 2004; *Lointier et al.*, 2013; *Takahashi et al.*, 2014; *Sheeley et al.*, 2001] can mainly be attributed to the methods employed by the previous studies, which neglect the presence of an equatorial peak in electron density. The key features of the empirical electron density model are now presented, discussing dependences of the model parameters on *L* and MLT.

*Cummings et al.* [1969] first modeled the electron density distribution along field lines as a power law form (equation (1)), as discussed in section 1, assuming a dipolar field and hydrogen plasma. The power law index, $\alpha$, is an important parameter, as it determines the rate at which electron density increases toward the ionospheric ends of the field line. For a diffusive equilibrium model, where the hydrostatic approximation is assumed, the number density along a flux tube is proportional to the magnetic field strength, which implies a power law index within the range of 0.5–1.0 [*Takahashi et al.*, 2004]. This diffusive equilibrium model is appropriate for high-density regions, such as the plasmasphere, where the hydrostatic approximation is valid. Low-density regions, such as the plasmatrough, can be suitably represented by a collisionless plasma model, which corresponds to a power law index of approximately 4 [*Takahashi et al.*, 2004]. Observational evidence of a power law dependence for the electron density distribution along field lines in the plasmatrough shows that the variation has a form between that predicted by the diffusive equilibrium model and that predicted by the collisionless model [*Goldstein et al.*, 2001; *Denton et al.*, 2002, 2004]. For example, *Denton et al.* [2002] observed a power law index of 1.6–2.1 for the plasmatrough.

It can be seen from equation (3d) that the power law index, $\alpha$ is modeled to include the observed dependences on both MLT and *L*. These variations are illustrated in Figure 7a, which shows the value of $\alpha$ as a function of MLT and *L*. Equation (3d) and Figure 7a show that $\alpha$ is assumed to have a linear dependence on *L* with a sinusoidal variation, where the amplitude is independent of *L*. However, the phase has an *L* dependence, such that the peak in $\alpha$ moves from approximately noon toward dawn with increasing *L*. Dependences of the power law index with MLT have also been reported from previous studies, such as *Denton et al.* [2002]. This result is consistent with the assumption that the power law form models the loading of electron density along field lines from the ionosphere. Due to electron outflows from photoionization at the ionosphere by incident solar radiation, the electron density is at a maximum at the ionospheric ends of the field line and decreases away from this region toward the equator. Therefore, the electron outflow will be greater on the dayside field lines, compared to the nightside field line footprints with reduced insolation, so the density at the footprints will be greater on the dayside. Consequently, this results in an increased magnitude of the gradient in electron density from the ends of the field line toward the magnetic equator for dayside field lines, so the observed $\alpha$ value should be greater for the dayside MLT sector. This is consistent with the determined value for the model $\alpha$ parameter.

Another feature of the $\alpha$ parameter is that the mean value of the variation is modeled to represent the observed increase of $\alpha$ with *L*, in agreement with previous findings [*Denton et al.*, 2002]. This is expected to be due to an increase in flux tube volume with *L*, such that the total electron density across the field lines is reduced. Therefore, for increased *L* values, the gradient in electron density from the end of a field line toward the magnetic equatorial plane will be increased in magnitude (i.e., a greater decrease in electron density moving away from the ionosphere), resulting in an increased $\alpha$ value. This feature of the $\alpha$ dependence is demonstrated in Figure 7a, where it can be seen that the magnitude of $\alpha$ increases with *L*. For the region modeled, $\alpha$ is approximately 0.4–1.0, which is markedly lower compared to other results previously mentioned [e.g., *Denton et al.*, 2002].

It is also assumed that $n_{e0}$ has a sinusoidal MLT variation, with the amplitude of the variation dependent on *L*, as illustrated by Figure 7b showing $n_{e0}$ as a function of MLT and *L*. In this case the phase of the sinusoidal variation was observed to be independent of *L*. The MLT dependence of $n_{e0}$ is found to have a maximum at approximately 1800 MLT, which is expected to be due to the "plasmaspheric bulge" [*Carpenter*, 1966; *Chappell et al.*, 1970]. This MLT dependence results in generally increased electron densities toward the duskside (in agreement with *Sheeley et al.* [2001]), which is clearly identified in Figure 7b as well as Figure 6a. However, it should be noted that our model is based on the full data set, averaged over all solar wind and geomagnetic conditions. This results in a blurring of the MLT variations presented in the equatorial distributions, as the plasmaspheric bulge shape and location is highly variable and dependent on various processes [*Carpenter*, 1970; *Chappell*, 1972; *Carpenter and Anderson*, 1992; *Gallagher et al.*, 2000; *Lointier et al.*, 2013].

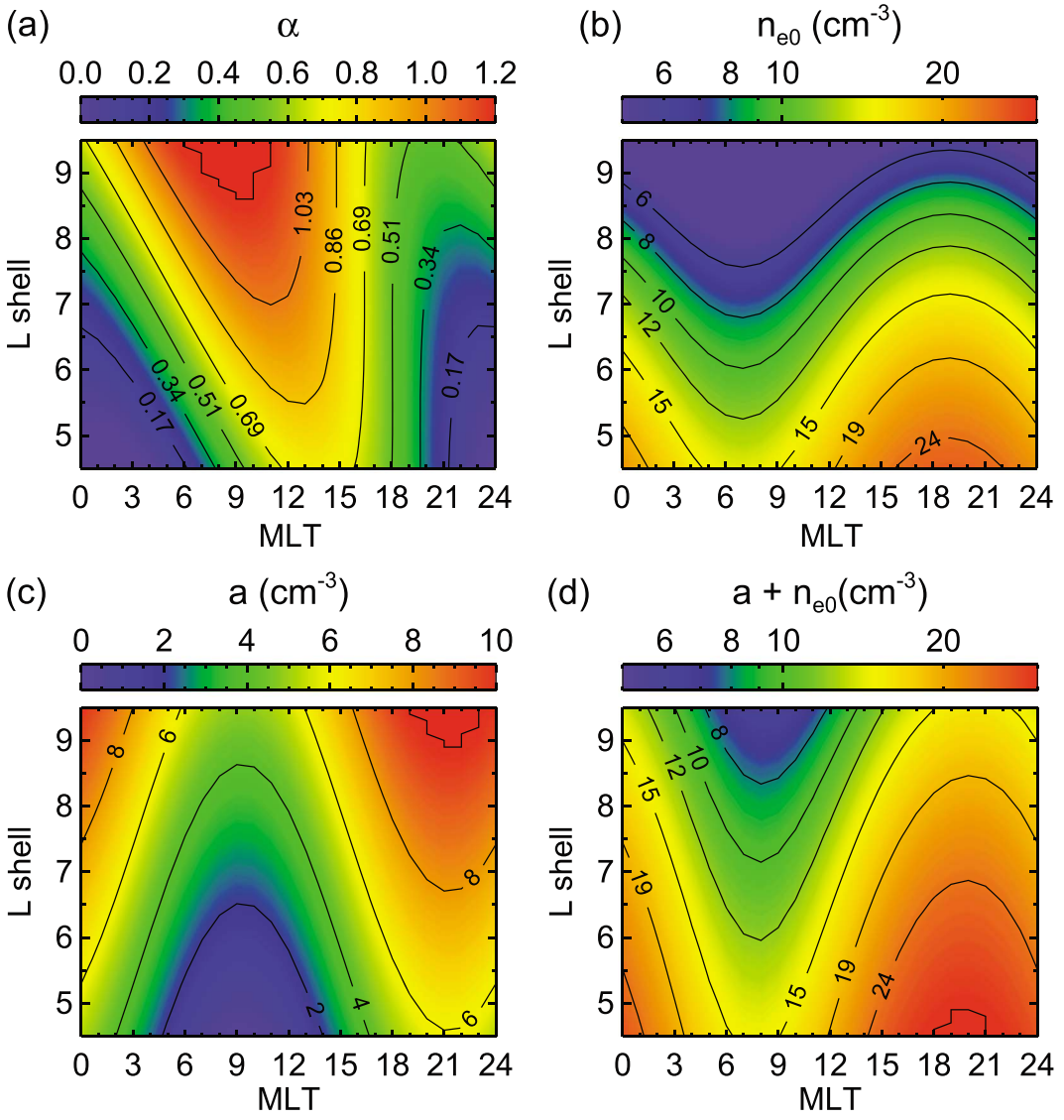


**Figure 7.** Contour plots showing the variation of the electron density parameters (as defined in equation (3)) with *L* value and MLT.

The amplitude of the MLT variation of $n_{e0}$ decreases with *L* shell, shown by Figure 7b and equation (3c). As mentioned above, the MLT dependence is due to the plasmaspheric bulge. Therefore, at increased *L* shells, further away from the plasmasphere boundary, the amplitude of the MLT variation is reduced.

In addition, the mean value of $n_{e0}$, averaged over sinusoidal variations, is found to decrease with the *L* value of the field line (apparent in Figure 7b), as previously observed [*Carpenter and Anderson*, 1992; *Goldstein et al.*, 2001; *Sheeley et al.*, 2001; *Denton et al.*, 2002, 2004; *Berube et al.*, 2005; *Ozhogin et al.*, 2012]. This could be a result of increased flux tube volume with increasing *L* value, such that the electron refilling from the ionosphere is distributed over a greater volume and results in generally decreased electron density values. The flux tube length is also increased so, due to the average lifetime of the electrons, the flux tube will take longer to be fully replenished by the ionospheric source, and on average will contain fewer electrons close to the magnetic equator. This is in agreement with *Denton et al.* [2004], where results indicated that the time associated with flux tube refilling is increased with increasing *L* shell.

However, as discussed in section 4, the power law model is not an appropriate description of the density close to the magnetic equator. Instead, a Gaussian function, with an offset of $n_{e0}$, is chosen to represent the distribution in this region, where the peak height *a* varies with *L* and MLT. As with the previous parameters,

the peak height relative to the background power law distribution, $a$, is assumed to have a sinusoidal variation, with a constant phase, as shown by Figure 7c. It can be seen that $a$ increases with $L$, such that the contribution of the Gaussian distribution at the magnetic equatorial plane increases for larger $L$. The MLT dependence of $a$ is such that the equatorial enhancement is strongest toward nightside field lines. Figure 7d shows the dependences of the total peak height, $a + n_{e0}$, on $L$ and MLT. The peak of this variation is located at approximately 1800 MLT, due to the MLT dependence of the $n_{e0}$ parameter (compare Figures 7b and 7d). It can also be seen from Figure 7d that the average value of the total peak height, $a + n_{e0}$, decreases with increasing $L$ value, where the decrease is dominated by the $n_{e0}$ dependence previously discussed.

It is important to consider that the equatorial region at high $L$ values, corresponding to observations of the equatorial peak, is only sampled in the later half of the time period covered by the WHISPER data set. This is due to variations in the orbital configuration, as the perigee gradually moved to higher latitudes throughout the time period considered in this study. In order to assess whether the observed equatorial enhancement is a consequence of the temporal variation in coverage, the field line distribution of electron density is examined further in Figure 8. Figure 8 (top) presents an example of the equatorial enhancement, observed for data within $8.5 \leq L < 9.5$ and $06 \pm 1.5$ MLT, and this $L$-MLT bin was chosen as a suitable case for further analysis. Figure 8 (middle) shows PEACE observations of the electron DNF (Differential Number Flux). The energy-pitch angle spectrogram shows an average of DNF observations obtained by the PEACE instrument on board the Cluster 1 spacecraft for the full time interval (2001–2012), for positions corresponding to $R_{norm} > 0.8$ within the $L$-MLT bin. Therefore, the results describe electrons in the equatorial enhancement region. It can be seen that for a given energy bin, the DNF distribution is not isotropic, and values are peaked for pitch angles close to 90°. This is known as a pancake pitch angle distribution, and referring to the particle distribution function for a collisionless plasma, implies that the number density of particles increases for decreasing magnetic field strength. This implies that the electron density approaches a maximum at the equatorial point of a field line, where the magnetic field is weakest, in agreement with the peaked distribution along the magnetic field observed in the WHISPER data set. As the pitch angle distribution shown in Figure 8 (middle) is based on complete energy-pitch angle spectrograms obtained by PEACE, the peaked distribution of electron density along the field lines can be attributed to an intrinsic property of the plasma, and therefore, the result provides support for the validity of the observed equatorial enhancement.

The distribution of electron density along the geomagnetic field can be further tested by separating the data set into two intervals, depending on the time of observation. The first interval covers the time period prior to October 2004, and the second interval covers observations obtained following October 2004. Therefore, the later time period corresponds to an interval during which the equatorial regions at high $L$ values were sampled, unlike the earlier time period. The reason for selecting October 2004 as the boundary between the two time periods is that the first interval corresponds to the temporal coverage of the CODIF data set. Figure 8 (bottom) shows the variation in electron density along a field line for the two intervals, where the first interval is indicated by the plus symbols and the second interval corresponds to the cross symbols. It can be concluded that the two profiles exhibit similar values in the region where there is concurrent data coverage, and in addition, the peaked distribution remains for the second time interval. Therefore, the equatorial enhancement, apparent in Figure 8 (top), is not a consequence of averaging data from different times, and the analysis indicates that the peaked distribution close to the magnetic equator is a valid feature. It is also important to note that the same features were present in the other $L$-MLT bins as for the case shown in Figure 8. Furthermore, the variations in the prominence of an equatorial enhancement with MLT and the initial decrease in electron density moving away from the magnetic equator forming a peaked distribution, would be unexplained assuming that the peak was a false result due to temporal variations in spatial coverage.

A possible explanation for the observed electron density peak near the magnetic equator in this data set could be the contribution of solar wind-magnetosphere coupling as an electron source (e.g., plasma entering the closed magnetosphere in the equatorial region, via the plasma sheet, through nightside reconnection processes). This peak is observed for the upper $L$ values of the considered region, where the electron input by photoionization at the ionosphere becomes comparable to the solar wind-magnetosphere coupling source. The density peak becomes increasingly prominent with increasing $L$ value, toward the plasma sheet region, due to the decreased background power law densities (representing a decreasing ionospheric contribution). This explanation also supports the MLT dependence of the height of the peak, as the ionospheric electron source is correlated with solar illumination, and so the dominance of the plasma sheet source is expected to be apparent for nightside field lines, where the plasma sheet becomes an important plasma source.

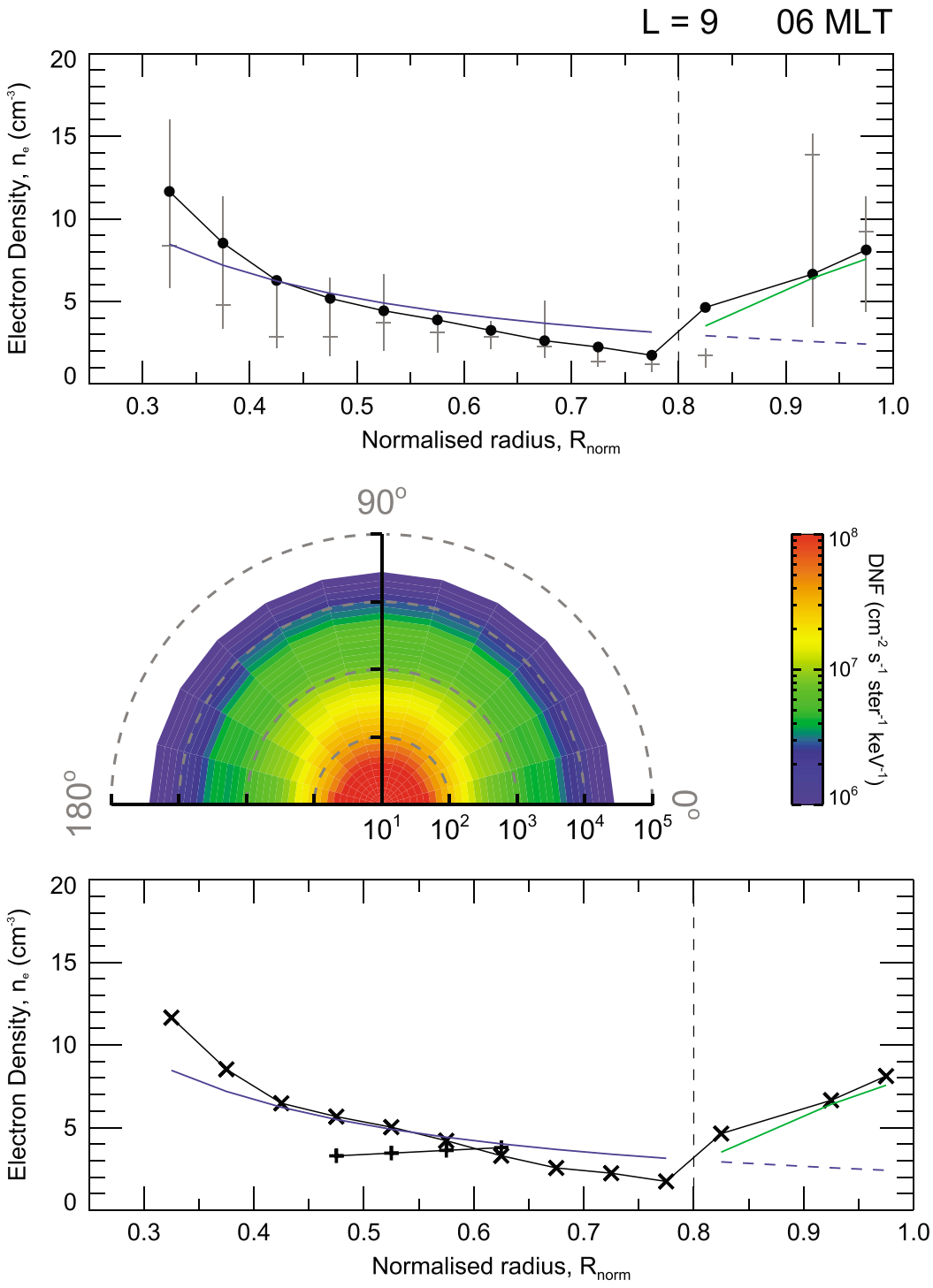


**Figure 8.** Data corresponding to 8.5 ≤ $L$ < 9.5 and 06 ± 1.5 MLT. Figure 8 (top and bottom) show the averaged WHISPER observations of electron density, $n_e$, plotted as a function of normalized radius, $R_{norm}$, using the same format as Figure 4. Figure 8 (top) corresponds to averaged values over the full WHISPER data set, reproduced for convenience from Figure 4. Figure 8 (bottom) shows the profile along the field line for data obtained before October 2004, represented by the plus symbols, and data obtained following October 2004, represented by the cross symbols. Figure 8 (middle) shows the average electron DNF (Differential Number Flux), $cm^{-2}$ $s^{-1}$ $ster^{-1}$ $keV^{-1}$, observed by the PEACE instrument onboard the Cluster 1 spacecraft, in an energy-pitch angle spectrogram. The radial and angular position of a given bin corresponds to the energy and pitch angle, respectively.

Flux tubes on the nightside are observed to have a decreased ionospheric plasma contribution due to reduced solar illumination, and plasma entry into the closed magnetosphere by reconnection primarily occurs on the nightside, increasing the contribution of the plasma sheet population.

Previous studies examining the electron density distribution along field lines in the plasmatrough region have observed a power law dependence with a density minimum at the magnetic equator [*Décréau et al.*, 1986; *Olsen et al.*, 1987; *Olsen*, 1992; *Denton et al.*, 2002, 2004], in contradiction with the results of this data set. It is important to note that these studies have limitations due to orbital configuration that may have inhibited the detection of an equatorial enhancement. The studies conducted by *Décréau et al.* [1986], *Olsen et al.* [1987], and *Olsen* [1992] were based on measurements from the DE-1 (Dynamics Explorer 1) instrument, which did not provide observations of the electron density distribution along field lines above $L \sim 6$. *Denton et al.* [2002] and *Denton et al.* [2004] used observations from the Polar spacecraft, which provide a lack of coverage at low latitudes for large $L$ values. The empirical model presented here indicates that the localized enhancement in electron density is prominent at large $L$ values, close to the magnetic equatorial plane, suggesting that some previous studies may have been unable to observe deviations from the expected power law dependence due to data coverage limitations. However, *Gallagher et al.* [2000] reported an increase in the sum of the $H^+$ and $He^+$ densities within approximately 20° of the magnetic equator, which, assuming quasi-neutrality, implies a corresponding maximum in electron density. This assumes that the contribution of other ion species in terms of number density is negligible, which is reasonable for the higher $L$ shells [see *Sandhu et al.*, 2016, Figure 8]. A possible localized peak was also examined by *Denton et al.* [2006], who concluded, from an analysis of CRRES plasma wave data, that there is no convincing evidence for a local peak in electron density near the magnetic equator. However, the results show insufficient data at low latitudes for large $L$ shells. In addition, *Denton et al.* [2006] noted a small peak for $L = 8–9$ but argued that at this range the magnetic latitude coverage is not complete, the magnetic field model is unreliable, and large statistical errors are present. In contrast to the evidence suggesting an electron density minimum, a case study conducted by *Denton et al.* [2009] observed a plasmatrough field line distribution of electron density with a localized peak at the magnetic equator, decreasing to a minimum value at a magnetic latitude of approximately 12.5°, then increasing steeply away from the magnetic equator. This appears to be the only conclusive observation of a peaked distribution in agreement with this empirical model.

### 5.2. Mass Density

The plasma number density is an important contribution to determining the total plasma mass density. This section will now explore how combining the empirical electron density model, representing the number density, with the average ion mass empirical model of *Sandhu et al.* [2016], describing the ion composition, can provide an estimation of the total plasma mass density distribution in the closed magnetosphere. Using the same approach as for the empirical electron density model, observations of ion densities from the CODIF instrument on board Cluster provided measurements of the average ion mass for the local plasma, which were empirically modeled by *Sandhu et al.* [2016]. The resulting empirical model for the distribution of average ion mass along field lines, included dependences on $L$ and MLT, covering all MLT sectors for the region of $5.9 \leq L < 9.5$. The key features of the model are the power law dependence used to describe variations along magnetic field lines, such that the average ion mass values maximize toward the magnetic equatorial plane, and enhanced values toward the nightside at lower $L$ values, mainly attributed the contribution of high-latitude heavy ion outflows convecting to the inner magnetosphere.

To estimate the total plasma mass density, for the region represented by both the empirical electron density model and the empirical average ion mass model, the following approach is taken. Using the spatial distributions of electron density, $n_e$, and average ion mass, $m_{av}$, a corresponding spatial distribution of the total plasma mass density, $\rho$, can be inferred from the relation

$$\rho = n_e m_{av} \tag{4}$$

which assumes that the magnetospheric plasma is quasi-neutral and the electron mass is negligible in comparison to the ion mass. In order to represent the full particle energy distribution of the magnetospheric plasma, this method of independently determining the number density and the average ion mass is chosen. This is because the resonance sounding technique used by the WHISPER instrument provides measurements of the total electron density for the plasma. The average ion mass determined from measurements by the CODIF instrument may be taken to represent the total plasma, reasonably assuming that the average ion mass is not a strong function of ion energy for the regions considered, as discussed by *Sandhu et al.* [2016].

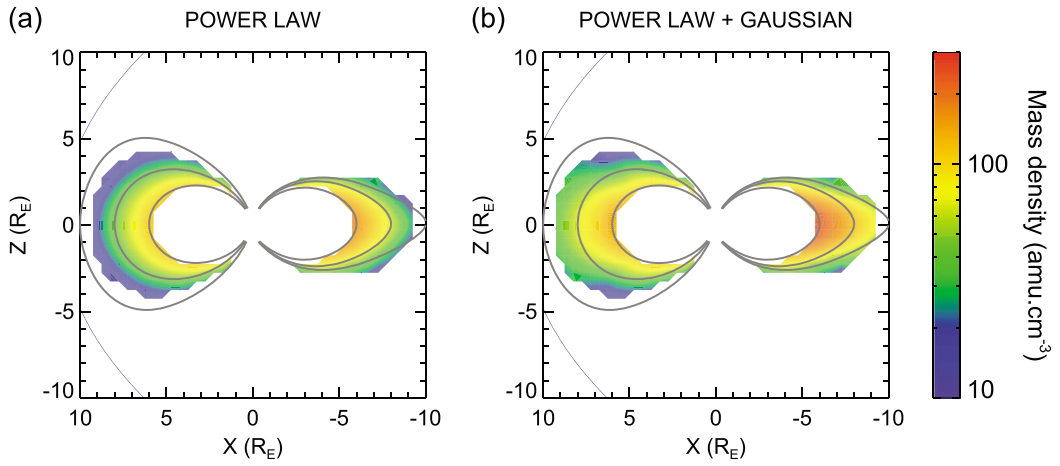


**Figure 9.** The spatial distribution of total plasma mass density (amu $cm^{-3}$) in the *X-Z* SM plane, corresponding to the electron density distributions shown in Figure 5.

The total plasma mass density is estimated using equation (4), and, from the range of *L* shells covered by both the electron density and average ion mass empirical models, the inferred empirical model for the total plasma mass density represents $5.9 \leq L < 9.5$. The resulting mass density empirical model includes contributions of the plasma number density and ion composition to the spatial variations. First, the combination of the electron density and average ion mass models to provide the mass density distribution in the *X-Z* SM plane is presented in Figure 9, where all values have been azimuthally mapped and averaged over MLT. As for the corresponding electron density distribution (Figure 5), both forms of the electron density model at low latitudes are considered for comparison. It can be seen from Figure 9b that the contribution of the localized electron density peak at the magnetic equatorial plane results in a clear enhancement of mass density compared to the case where this is neglected (Figure 9a), particularly at larger *L* values.

The corresponding mass density distribution in the T96 equatorial plane is shown in Figure 10, demonstrating dependences with *L* and MLT. As expected, the use of the Gaussian function to represent the electron density equatorial peak results in comparatively enhanced mass density values. It can also be noted here that the contribution of the ion composition in this region is also an important factor in determining the mass density distribution, as shown by a comparison of Figure 5 with Figure 9, and Figure 6 with Figure 10.

The variations of mass density in the equatorial plane are worthwhile discussing. Figure 10 illustrates the *L* dependence of the inferred mass density model, with high mass density plasma present at low *L* values,

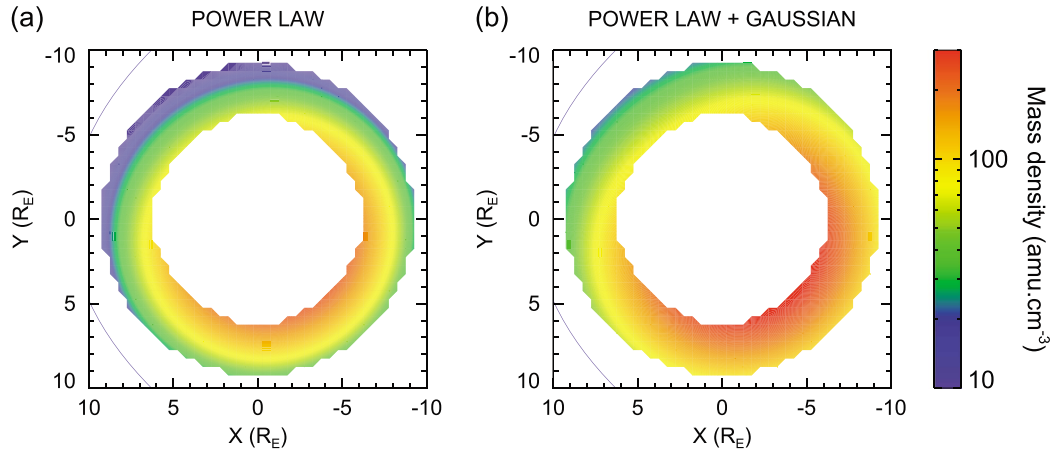


**Figure 10.** The spatial distribution of total plasma mass density (amu $cm^{-3}$) in the T96 magnetic equatorial plane, corresponding to the electron density distributions shown in Figure 6.

due to the average ion mass enhancement and high number density plasma. The mass density decreases with $L$ value, which is attributed to decreasing plasma number density as a result of larger flux tube volume and length. The composition of the plasma also becomes less $O^+$ dominated, resulting in decreasing mass density. In general, the decrease in mass density with $L$ is in agreement with previous models [*Takahashi et al.*, 2004; *Denton et al.*, 2006; *Maeda et al.*, 2009; *Min et al.*, 2013; *Takahashi et al.*, 2014].

Figure 10 demonstrates the MLT dependence of the mass density model. It can be seen that the equatorial mass density approaches a maximum in the evening sector. By considering the electron density enhancement at approximately 1900 MLT, due to the duskside plasmaspheric bulge region, and the average ion mass enhancement due to the plasma sheet population present for nightside field lines [*Sandhu et al.*, 2016], it is clear that the mass density enhancement in this region is due to a combination of both features. Therefore, the variation in mass density with MLT is due to contributions from both the number density and ion composition.

Furthermore, it is also of interest to consider variations along the geomagnetic field in the total mass density. Previous studies suggest that the dependence along field lines of mass density is expected to have a relatively flat profile (small positive power law index) for lower $L$ values [*Takahashi et al.*, 2004; *Denton et al.*, 2006; *Maeda et al.*, 2009]; whereas at larger $L$ values, previous studies find that the distribution is locally peaked at the magnetic equatorial plane, decreases off equator, and then increases again toward the ionospheric ends of the field lines [*Takahashi et al.*, 2004; *Denton et al.*, 2006; *Takahashi and Denton*, 2007; *Denton et al.*, 2009]. The distribution of the inferred mass density along field lines and variations with $L$ value and MLT are now discussed, considering the high latitude and equatorial regions separately.

By combining the electron density and average ion mass empirical models, the profiles of mass density along field lines are determined. Examples of the profiles of mass density are shown in Figure 11. Figure 11 (left column) shows profiles for $L = 6$, and Figure 11 (right column) shows profiles for $L = 9$. Figure 11 (top row) shows profiles for 1200 MLT, and Figure 11 (bottom row) shows profiles for 0000 MLT. A comparison of these panels illustrate the dependences of the mass density distribution along the geomagnetic field with MLT and $L$. The corresponding profiles predicted by the electron density (defined by equation (3)) and average ion mass models (defined by equation 2 in *Sandhu et al.* [2016]) are also included in Figure 11, which illustrate the contributions of the plasma number density and ion composition to the mass density distribution along magnetic field lines.

The results indicate that the high-latitude region (at $R_{norm} \leq 0.8$) generally demonstrates a power law dependence of mass density along the geomagnetic field. For dayside field lines (see Figure 11, top row) the off-equator high-latitude region shows an increasing mass density toward the ionospheric ends of the field line, indicating a power law dependence with a positive power law index, similar to the electron density distribution. As for the electron density, the power law index is shown to become more positive for larger $L$ values on the dayside (note that a comparison of Figure 11 (top row) does not clearly illustrate this feature, as the power law index actually represents the logarithmic gradient and linear axes have been used here), corresponding to steeper mass density profiles in the high-latitude region, in agreement with previous studies [*Denton et al.*, 2006; *Maeda et al.*, 2009]. The close correlation of the mass density field line distribution form with the observed electron density indicates that the mass density distribution at high latitudes along closed dayside field lines is dominated by the number density.

In contrast, the high-latitude region of the nightside field lines exhibits differing features. Referring to Figure 11 (bottom row), the field line profile at lower $L$ values show the mass density decreasing toward the ends of the field line, represented by a negative power law index similarly to the average ion mass distribution. Moving to larger $L$ values, the profile becomes flatter, as the power law index increases and becomes positive for this region. This results in a distribution where the mass density increases slightly toward the ionospheric ends of the field lines, in agreement with the observed electron density field line distribution. Therefore, it can be inferred that the nightside mass density distribution at high latitudes is dominated by the ion composition at lower $L$ values and becomes increasingly dominated by the number density at larger $L$ values. As for the dayside field lines, the increase in the power law index is roughly consistent with previous studies [*Denton et al.*, 2006; *Maeda et al.*, 2009], although these studies constrain the power law index to be positive. This approach considers negative power law index values to account for the effects of the centrifugal force on heavy ions.

The consideration of the profiles shown in Figure 11 indicate that the number density is generally the dominant factor in determining the high-latitude distribution of mass density along field lines. An exception to this

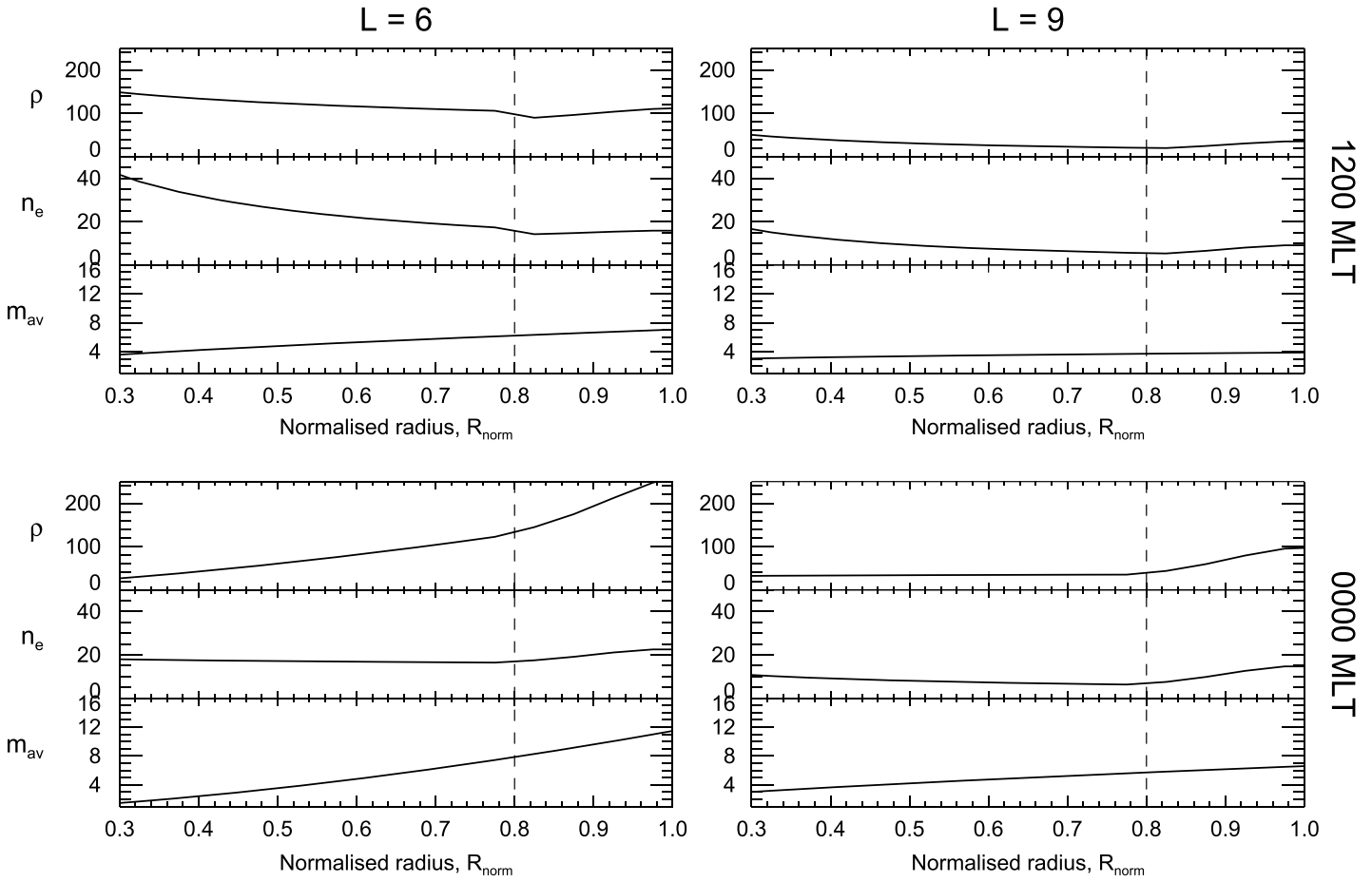


**Figure 11.** Panels showing the mass density, $\rho$ (amu cm$^{-3}$), electron density, $n_e$ (cm$^{-3}$) as defined by equation (3), and average ion mass, $m_{av}$ (amu) as defined by equation 2 in *Sandhu et al.* [2016], plotted as a function of normalized radius, $R_{norm}$. The panels show profiles for (left column) $L = 5$, (right column) $L = 9$, (top row) 1200 MLT, and (bottom row) 0000 MLT. The vertical dashed line on each panel indicates the boundary between the power law and Gaussian dependences, corresponding to the electron density model.

is at lower $L$ values on nightside MLT sectors (see Figure 11, bottom left), where the ion composition appears to be the dominant contribution to the mass density. This is expected to correspond to the presence of the average ion mass enhancement at the lower $L$ values, and the average ion mass field line profile is steepest (most negative power law index) with a peak in the equatorial average ion mass at approximately 2100–2200 MLT [*Sandhu et al.*, 2016]. Therefore, in the nightside region at lower $L$ values, the plasma is relatively $O^+$ rich and the ion composition has a significant contribution to the mass density. Moving away from this average ion mass enhancement, the relative concentration of $O^+$ ions decreases and the field line profiles become flatter, resulting in a decreased contribution of the ion composition.

The resulting mass density distribution along the field lines also presents some notable features for the low-latitude equatorial region (at $R_{norm} > 0.8$), illustrated in the example profiles shown in Figure 11. The combination of the localized electron density peak with the average ion mass, which approaches a maximum toward the magnetic equatorial plane, provides a peaked mass density distribution at the equator, as expected. The low-latitude peak, in comparison to the expected low-latitude distribution extrapolated from the high-latitude region, is observed to become increasingly prominent at larger $L$ values, in agreement with previous findings [*Takahashi et al.*, 2004; *Denton et al.*, 2006; *Takahashi and Denton*, 2007; *Denton et al.*, 2009]. This can be attributed to the contribution of the plasma number density, as the localized electron density peak height (relative to the background power law distribution) increases with $L$, which is illustrated by a comparison of the predicted mass density distributions shown in Figure 9. It can be seen that the mass density distribution corresponding to the use of the Gaussian function at low latitudes, as opposed to the extrapolated power law dependence, results in noticeably increased values near the magnetic equatorial plane at

larger $L$ values. This contradicts previous studies [*Takahashi et al.*, 2004; *Denton et al.*, 2006; *Takahashi and Denton*, 2007], where the equatorial mass density peak has predominantly been associated with a low-latitude enhancement of heavy ions, under the assumption that the electron density follows a power law dependence. Whereas the results of this study appear to indicate that a localized peak in the number density is also a significant factor to the mass density in this region.

## 6. Conclusions and Further Work

This study has determined an empirical model for the distribution of electron density along closed geomagnetic field lines, including dependences on $L$ shell and MLT. The empirical model is based on observations obtained by the WHISPER instrument on board Cluster, for a time interval spanning approximately 2001–2012. A key result obtained is the presence of a localized peak in electron density close to the magnetic equator in the electron density model, unaccounted for by many previous models. The spatial variations in electron density provide useful insight into the plasma loading processes occurring in this region, and their dependencies with $L$ and MLT. A key features of this model, compared to previous empirical models, is the size and coverage of the underlying data sets. Furthermore, the observed localized enhancement in the plasma number density close to the magnetic equatorial plane is accounted for. Future developments of the empirical electron density model include considering variations in the spatial distribution with different parameters and indices, representing solar wind and geomagnetic dependences.

This study also considered how the combination of the empirical electron density model with an empirical model for the average ion mass can be used to infer the spatial distribution of the plasma mass density between $5.9 \leq L < 9.5$. The results illustrate how the contributions of plasma number density and ion composition determine the total plasma mass density and how the relative contributions are spatially dependent. An area of future work includes the application of this mass density model to examine the properties of standing Alfvén waves on closed geomagnetic field lines using a time-of-flight technique, continuing the study of *Wild et al.* [2005]. This will provide information on how plasma mass loading of the magnetic field lines influences Alfvén pulsation frequencies.

**Acknowledgments**

J.K.S. is supported by STFC studentship ST/K502121, T.K.Y. is supported by STFC grant ST/H002480/1, and R.C.F. is supported by STFC Ernest Rutherford FellowshipST/K004298/1. The authors would like to thank the WHISPER and CIS PIs and instrument teams, and the CAA (http://caa.estec.esa.int/caa/home.xml) for providing the Cluster data used. French participation in the Cluster project is funded by CNES. We also thank the referees for their constructive comments. OMNI data were obtained from the NASA/GSFC OMNIWeb interface (http://omniweb.gsfc.nasa.gov). The *Dst* index data were obtained from the World Data Center for Geomagnetism, Kyoto (http://wdc.kugi.kyoto-u.ac.jp/dstae/index.html). The data underlying this study are freely available from the above archives. The analysis code used in this study is stored in the University of Leicester computer systems and is available on request.

## References

Berube, D., M. B. Moldwin, S. F. Fung, and J. L. Green (2005), A plasmaspheric mass density model and constraints on its heavy ion concentration, *J. Geophys. Res.*, *110*, A04212, doi:10.1029/2004JA010684.

Borovsky, J. E., and M. H. Denton (2006), Effect of plasmaspheric drainage plumes on solar-wind/magnetosphere coupling, *Geophys. Res. Lett.*, *33*, L20101, doi:10.1029/2006GL026519.

Carpenter, D. L. (1966), Whistler studies of the plasmapause in the magnetosphere: 1. Temporal variations in the position of the knee and some evidence on plasma motions near the knee, *J. Geophys. Res.*, *71*, 693–709, doi:10.1029/JZ071i003p00693.

Carpenter, D. L. (1970), Whistler evidence of the dynamic behavior of the duskside bulge in the plasmasphere, *J. Geophys. Res.*, *75*, 3837–3847, doi:10.1029/JA075i019p03837.

Carpenter, D. L., and R. R. Anderson (1992), An ISEE/Whistler model of equatorial electron density in the magnetosphere, *J. Geophys. Res.*, *97*, 1097–1108, doi:10.1029/91JA01548.

Chappell, C. R. (1972), Recent satellite measurements of the morphology and dynamics of the plasmasphere, *Rev. Geophys.*, *10*, 951–979, doi:10.1029/RG010i004p00951.

Chappell, C. R., K. K. Harris, and G. W. Sharp (1970), The morphology of the bulge region of the plasmasphere, *J. Geophys. Res.*, *75*, 3848, doi:10.1029/JA075i019p03848.

Clark, J., and A. Gelfand (2006), *Hierarchical Modelling for the Environmental Sciences: Statistical Methods and Applications*, Oxford biology, Oxford Univ. Press, U. K.

Clausen, L. B. N., T. K. Yeoman, R. C. Fear, R. Behlke, E. A. Lucek, and M. J. Engebretson (2009), First simultaneous measurements of waves generated at the bow shock in the solar wind, the magnetosphere and on the ground, *Ann. Geophys.*, *27*, 357–371, doi:10.5194/angeo-27-357-2009.

Cummings, W. D., R. J. O'Sullivan, and P. J. Coleman Jr. (1969), Standing Alfvén waves in the magnetosphere, *J. Geophys. Res.*, *74*, 778, doi:10.1029/JA074i003p00778.

Décréau, P. M. E., D. Carpenter, C. R. Chappell, J. Green, and J. H. Waite Jr. (1986), Latitudinal plasma distribution in the dusk plasmaspheric bulge—Refilling phase and quasi-equilibrium state, *J. Geophys. Res.*, *91*, 6929–6943, doi:10.1029/JA091iA06p06929.

Décréau, P. M. E., et al. (1997), Whisper, a resonance sounder and wave analyser: Performances and perspectives for the Cluster mission, *Space Sci. Rev.*, *79*, 157–193, doi:10.1023/A:1004931326404.

Denton, R. E., J. Goldstein, J. D. Menietti, and S. L. Young (2002), Magnetospheric electron density model inferred from Polar plasma wave data, *J. Geophys. Res.*, *107*, 1386, doi:10.1029/2001JA009136.

Denton, R. E., J. D. Menietti, J. Goldstein, S. L. Young, and R. R. Anderson (2004), Electron density in the magnetosphere, *J. Geophys. Res.*, *109*, A09215, doi:10.1029/2003JA010245.

Denton, R. E., K. Takahashi, I. A. Galkin, P. A. Nsumei, X. Huang, B. W. Reinisch, R. R. Anderson, M. K. Sleeper, and W. J. Hughes (2006), Distribution of density along magnetospheric field lines, *J. Geophys. Res.*, *111*, A04213, doi:10.1029/2005JA011414.

Denton, R. E., et al. (2009), Field line distribution of density at $L = 4.8$ inferred from observations by CLUSTER, *Ann. Geophys.*, *27*, 705–724, doi:10.5194/angeo-27-705-2009.

Escoubet, C. P., R. Schmidt, and M. L. Goldstein (1997a), Cluster—Science and mission overview, *Space Sci. Rev.*, *79*, 11–32, doi:10.1023/A:1004923124586.

Escoubet, C. P., A. Pedersen, R. Schmidt, and P. A. Lindqvist (1997b), Density in the magnetosphere inferred from ISEE 1 spacecraft potential, *J. Geophys. Res.*, *102*, 17,595–17,610, doi:10.1029/97JA00290.

Fung, S. F., L. N. Garcia, J. L. Green, D. L. Gallagher, D. L. Carpenter, B. W. Reinisch, I. A. Galkin, G. Khmyrov, and B. R. Sandel (2001), Plasmaspheric electron density distributions sampled by radio plasma imager on the IMAGE satellite, *Eos Trans. AGU*, *82*(47), Fall Meet. Suppl., Abstract SM11A-0771.

Gallagher, D. L., P. D. Craven, and R. H. Comfort (2000), Global core plasma model, *J. Geophys. Res.*, *105*, 18,819–18,834, doi:10.1029/1999JA000241.

Goldstein, J., R. E. Denton, M. K. Hudson, E. G. Miftakhova, S. L. Young, J. D. Menietti, and D. L. Gallagher (2001), Latitudinal density dependence of magnetic field lines inferred from Polar plasma wave data, *J. Geophys. Res.*, *106*, 6195–6202, doi:10.1029/2000JA000068.

Gustafsson, G., et al. (1997), The electric field and wave experiment for the cluster mission, *Space Sci. Rev.*, *79*, 137–156, doi:10.1023/A:1004975108657.

Gustafsson, G., et al. (2001), First results of electric field and density observations by Cluster EFW based on initial months of operation, *Ann. Geophys.*, *19*, 1219–1240, doi:10.5194/angeo-19-1219-2001.

Johnstone, A. D., et al. (1997), Peace: A plasma electron and current experiment, *Space Sci. Rev.*, *79*, 351–398, doi:10.1023/A:1004938001388.

Laakso, H., and A. Pedersen (1998), *Ambient Electron Density Derived From Differential Potential Measurements, Geophys. Monogr. Ser.*, 102, vol. 49, AGU, Washington, D. C.

Laakso, H., R. Pfaff, and P. Janhunen (2002), Polar observations of electron density distribution in the Earth's magnetosphere. 1. Statistical results, *Ann. Geophys.*, *20*, 1711–1724, doi:10.5194/angeo-20-1711-2002.

Lointier, G., F. Darrouzet, P. M. E. Décréau, X. Vallières, S. Kougblénou, J. G. Trotignon, and J.-L. Rauch (2013), Refilling process in the plasmasphere: A 3-D statistical characterization based on Cluster density observations, *Ann. Geophys.*, *31*, 217–237, doi:10.5194/angeo-31-217-2013.

Lybekk, B., A. Pedersen, S. Haaland, K. Svenes, A. N. Fazakerley, A. Masson, M. G. G. T. Taylor, and J.-G. Trotignon (2012), Solar cycle variations of the Cluster spacecraft potential and its use for electron density estimations, *J. Geophys. Res.*, *117*, A01217, doi:10.1029/2011JA016969.

Maeda, N., S. Takasaki, H. Kawano, S. Ohtani, P. Decreau, J. Trotignon, S. Solovyev, D. Baishev, and K. Yumoto (2009), Simultaneous observations of the plasma density on the same field line by the CPMN ground magnetometers and the Cluster satellites, *Adv. Space Res.*, *43*, 265–272, doi:10.1016/j.asr.2008.04.016.

Meredith, N. P., R. M. Thorne, R. B. Horne, D. Summers, B. J. Fraser, and R. R. Anderson (2003), Statistical analysis of relativistic electron energies for cyclotron resonance with EMIC waves observed on CRRES, *J. Geophys. Res.*, *108*, 1250, doi:10.1029/2002JA009700.

Min, K., J. Bortnik, R. E. Denton, K. Takahashi, J. Lee, and H. J. Singer (2013), Quiet time equatorial mass density distribution derived from AMPTE/CCE and GOES using the magnetoseismology technique, *J. Geophys. Res. Space Physics*, *118*, 6090–6105, doi:10.1002/jgra.50563.

Nakagawa, T., T. Ishii, K. Tsuruda, H. Hayakawa, and T. Mukai (2000), Net current density of photoelectrons emitted from the surface of the GEOTAIL spacecraft, *Earth Planets Space*, *52*, 283–292.

O'Brien, T. P., K. R. Lorentzen, I. R. Mann, N. P. Meredith, J. B. Blake, J. F. Fennell, M. D. Looper, D. K. Milling, and R. R. Anderson (2003), Energization of relativistic electrons in the presence of ULF power and MeV microbursts: Evidence for dual ULF and VLF acceleration, *J. Geophys. Res.*, *108*, 1329, doi:10.1029/2002JA009784.

Olsen, R. C. (1992), The density minimum at the Earth's magnetic equator, *J. Geophys. Res.*, *97*, 1135–1150, doi:10.1029/91JA02719.

Olsen, R. C., S. D. Shawhan, D. L. Gallagher, C. R. Chappell, and J. L. Green (1987), Plasma observations at the Earth's magnetic equator, *J. Geophys. Res.*, *92*, 2385–2407, doi:10.1029/JA092iA03p02385.

Ozhogin, P., J. Tu, P. Song, and B. W. Reinisch (2012), Field-aligned distribution of the plasmaspheric electron density: An empirical model derived from the IMAGE RPI measurements, *J. Geophys. Res.*, *117*, A06225, doi:10.1029/2011JA017330.

Pedersen, A. (1995), Solar wind and magnetosphere plasma diagnostics by spacecraft electrostatic potential measurements, *Ann. Geophys.*, *13*, 118–129, doi:10.1007/s00585-995-0118-8.

Pedersen, A., et al. (2001), Four-point high time resolution information on electron densities by the electric field experiments (EFW) on Cluster, *Ann. Geophys.*, *19*, 1483–1489, doi:10.5194/angeo-19-1483-2001.

Pedersen, A., et al. (2008), Electron density estimations derived from spacecraft potential measurements on Cluster in tenuous plasma regions, *J. Geophys. Res.*, *113*, doi:10.1029/2007JA012636.

Rème, H., et al. (1997), The Cluster Ion Spectrometry (CIS) experiment, *Space Sci. Rev.*, *79*, 303–350, doi:10.1023/A:1004929816409.

Sandhu, J. K., T. K. Yeoman, R. C. Fear, and I. Dandouras (2016), A statistical study of magnetospheric ion composition along the geomagnetic field using the Cluster spacecraft for L values between 5.9 and 9.5, *J. Geophys. Res. Space Physics*, *121*, 2194–2208, doi:10.1002/2015JA022261.

Scudder, J. D., X. Cao, and F. S. Mozer (2000), Photoemission current-spacecraft voltage relation: Key to routine, quantitative low-energy plasma measurements, *J. Geophys. Res.*, *105*, 21,281–21,294, doi:10.1029/1999JA900423.

Sheeley, B. W., M. B. Moldwin, H. K. Rassoul, and R. R. Anderson (2001), An empirical plasmasphere and trough density model: CRRES observations, *J. Geophys. Res.*, *106*, 25,631–25,642, doi:10.1029/2000JA000286.

Tabachnick, B. G., and L. S. Fidell (2006), *Using Multivariate Statistics*, 5th ed., Allyn & Bacon, Inc., Needham Heights, Mass.

Takahashi, K., and R. E. Denton (2007), Magnetospheric seismology using multiharmonic toroidal waves observed at geosynchronous orbit, *J. Geophys. Res.*, *112*, A05204, doi:10.1029/2006JA011709.

Takahashi, K., R. E. Denton, R. R. Anderson, and W. J. Hughes (2004), Frequencies of standing Alfvén wave harmonics and their implication for plasma mass distribution along geomagnetic field lines: Statistical analysis of CRRES data, *J. Geophys. Res.*, *109*, A08202, doi:10.1029/2003JA010345.

Takahashi, K., R. E. Denton, M. Hirahara, K. Min, S.-I. Ohtani, and E. Sanchez (2014), Solar cycle variation of plasma mass density in the outer magnetosphere: Magnetoseismic analysis of toroidal standing Alfvén waves detected by Geotail, *J. Geophys. Res. Space Physics*, *119*, 8338–8356, doi:10.1002/2014JA020274.

Trotignon, J. G., et al. (2001), How to determine the thermal electron density and the magnetic field strength from the Cluster/Whisper observations around the Earth, *Ann. Geophys.*, *19*, 1711–1720, doi:10.5194/angeo-19-1711-2001.

Trotignon, J. G., J. L. Rauch, P. M. E. Décréu, P. Canu, and J. Lemaire (2003), Active and passive plasma wave investigations in the Earth's environment: The Cluster/Whisper experiment, *Adv. Space Res.*, *31*, 1449–1454, doi:10.1016/S0273-1177(02)00959-6.

Tsyganenko, N. A. (1996), Effects of the solar wind conditions in the global magnetospheric configurations as deduced from data-based field models (Invited), in *Proceedings of the 3rd International Conference held in Versailles, International Conference on Substorms*, vol. 389, pp. 181–185, edited by E. J. Rolfe and B. Kaldeich, ESA Special Publ., Paris.

Wild, J. A., T. K. Yeoman, and C. L. Waters (2005), Revised time-of-flight calculations for high-latitude geomagnetic pulsations using a realistic magnetospheric magnetic field model, *J. Geophys. Res.*, *110*, A11206, doi:10.1029/2004JA010964.